Heliyon 10 (2024) e29957

Contents lists available at ScienceDirect

Heliyon

journal homepage: www.cell.com/heliyon

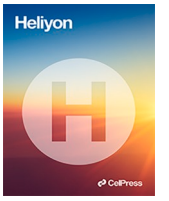

Research article

Preparation of a hierarchical porous activated carbon derived from cantaloupe peel/fly ash/PEDOT:PSS composites as Pt-free counter electrodes of dye-sensitized solar cells

Nattakan Kanjana [a,b], Wasan Maiaugree [a,c,*], Tirapat Wechprasit [a,c], Anusit Kaewprajak [d], Pisist Kumnorkaew [d], Poramed Wongjom [c], Yingyot Infahsaeng [c,e]

[a] Thammasat University Research Unit in Energy Innovations and Modern Physics (EIMP), Thammasat University, Pathum Thani 12120, Thailand
[b] Faculty of Agriculture and Technology, Rajamangala University of Technology Isan, Surin Campus, Surin 32000, Thailand
[c] Division of Physics, Faculty of Science and Technology, Thammasat University, Pathum Thani 12120, Thailand
[d] National Nanotechnology Center (NANOTEC), National Science and Technology Development Agency (NSTDA), Pathum Thani 12120, Thailand
[e] Thammasat University Research Unit in Quantum Technology Thammasat University, Pathum Thani 12120, Thailand

ARTICLE INFO

Keywords:
Fly ash
Activated carbon
Dye-sensitized solar cell
PEDOT:PSS
Counter electrodes

ABSTRACT

Hierarchical porous activated carbon/fly ash/PEDOT:PSS composites (AC:FA) for a counter electrode (CE) were created using a doctor blade technique and applied in dye sensitized solar cells. Hierarchical porous activated carbon (AC) was produced using a potassium hydroxide (KOH) activation process from cantaloupe peels (*Cucumis melo* L. var. cantaloupensis). AC was introduced into fly ash at various mass ratios to enhance several physical and electrochemical characteristics. Compared to bare FA, the AC:FA electrode displayed a high electrocatalytic activity for the iodide/triiodide redox (I^-/I_3^-) reaction. The test findings show that a higher proportion of AC has an impact on a CE's catalytic activity and charge transfer resistance. The power conversion efficiency (PCE) of the dye-sensitized solar cell (DSSC) attained 5.81 % using the AC:FA CE with AC in a mass ratio of FA in 3:1 (wt./wt.), which is very near the performance of manufactured DSSC's with a platinum (Pt)-based CE (5.91 %). The AC:FA CE stands out as a strong candidate to substitute for costly Pt CEs due to its enhanced electrochemical activity and charge transfer capabilities obtained with an inexpensive and simple production procedure.

1. Introduction

In recent years, DSSCs have received much interest as possible alternatives for sustainable energy generation. These devices have a number of benefits over typical silicon-based solar cells, including their lower production costs, flexibility, and the capability of capturing light from a variety of angles [1,2]. A CE is important in DSSCs because it catalyzes the reduction of redox species. Its function is to transport electrons from an external circuit to the redox electrolyte's triiodide and iodide [3,4]. The CE of a high-performance DSSC must be both catalytic and conductive. As a result, Pt, which is an excellent catalyst for the reduction of redox species such as I^-/I_3^-, is commonly utilized for CEs in DSSCs. However, the use of Pt presents challenges due to its high cost for

* Corresponding author.
E-mail address: wasankim@tu.ac.th (W. Maiaugree).

https://doi.org/10.1016/j.heliyon.2024.e29957
Received 18 December 2023; Received in revised form 21 February 2024; Accepted 18 April 2024
Available online 24 April 2024

large-scale production, limited availability, and environmental concerns [4,5].

This has prompted scientists to examine alternative materials that might deliver equivalent catalytic activity without compromising performance. Several Pt-free materials have been studied as potential counter electrode replacements in DSSCs. For example, carbon-based materials [6], including carbon spheres [7], activated carbon [3,8], carbon nanotubes [9], reduced graphene oxide (rGO) [10], and graphite [11,12], have been widely researched as Pt-free CE materials. They have strong electrical conductivity, high specific surface areas and can accelerate the reduction process of the redox pair in an electrolyte [13]. Conductive polymers such as polyaniline (PANI) [14], poly (3,4-ethylenedioxythiophene) (PEDOT) [15], poly (3,4-ethylenedioxythiophene) polystyrene sulfonate (PEDOT:PSS) [16] and polypyrrole [17,18] have also been investigated as Pt-free alternatives. These polymers have the benefit of being solution-processable, enabling low-cost and large-scale manufacture. However, their catalytic activity and long-term stability need improvement. Metal oxides with high electrocatalytic activity and stability include tungsten oxide (WO_3) [19], iridium dioxide (IrO_2) [20], molybdenum oxide (MoO_3) [21], and nickel oxide (NiO) [22] as well as sulfide catalyst materials such as molybdenum sulfide (MoS_2) and tungsten sulfide (WS_2) [23]. Additionally, composite materials combining carbon with other conductive materials, such as conducting polymers or metal nanoparticles, have been investigated. Composite materials have emerged as possible Pt-free counter electrodes in DSSCs in this context [10,24]. These composites have the potential to improve electrical conductivity and catalytic activity. Recently, a new tungsten disulfide-molybdenum copper oxide composite with graphene quantum dots (WM@GQDs) was developed by Areerob et al. as a counter electrode. Their WM@GQDs CE exhibited good efficiency (10.38 %) compared to that of Pt (10.26 %) [25]. Wu et al. synthesized Co_9S_8/NC@$FeCoS_2$/NC composites with a hollow yolk shell structured CE with a high specific surface area that provides numerous active sites and promotes contact between the electrolyte and catalytic sites, yielding a PCE of 7.07 % [26]. Zambrzycki et al. presented hierarchical carbon nanofiber/carbon nanotube/NiCo nanocomposites. A PCE of 7.08 % [27] was achieved as a result of this increased electrocatalytic activity for I_3^- reduction and rapid electron transfer. Srisuvetha et al. assembled a DSSC with an MgO/MWCNT composite as a CE and achieved a high PCE of 5.15 % [28]. The MoP/$MoNiP_2$@Ti_3C_2 composite counter electrode, developed by He et al., had a high solar cell efficiency of 10.01 % and demonstrated superior catalytic activity for the I^-/I_3^- redox reaction compared to platinized CEs (8.22 %) [29].

In this paper, we explore utilization of composite materials that combine activated carbon with fly ash and primarily consists of silicon dioxide (SiO_2), aluminum oxide (Al_2O_3), iron oxide (Fe_2O_3), calcium oxide (CaO), and small amounts of other oxides [16]. These may serve as sustainable and cost-effective alternatives for Pt-free counter electrodes in DSSCs. We discuss the unique properties of these composite materials, their electrocatalytic activity, and their potential to enhance the efficiency of DSSCs. An overall conversion efficiency of up to 5.81 % was obtained for DSSCs using the hierarchical porous activated carbon derived from cantaloupe peel/fly ash/PEDOT:PSS composite materials (AC:FA) and used as counter electrodes. This is comparable to the performance of Pt-based CEs (5.91 %), highlighting their potential to drive the realization of efficient and environmentally friendly DSSCs.

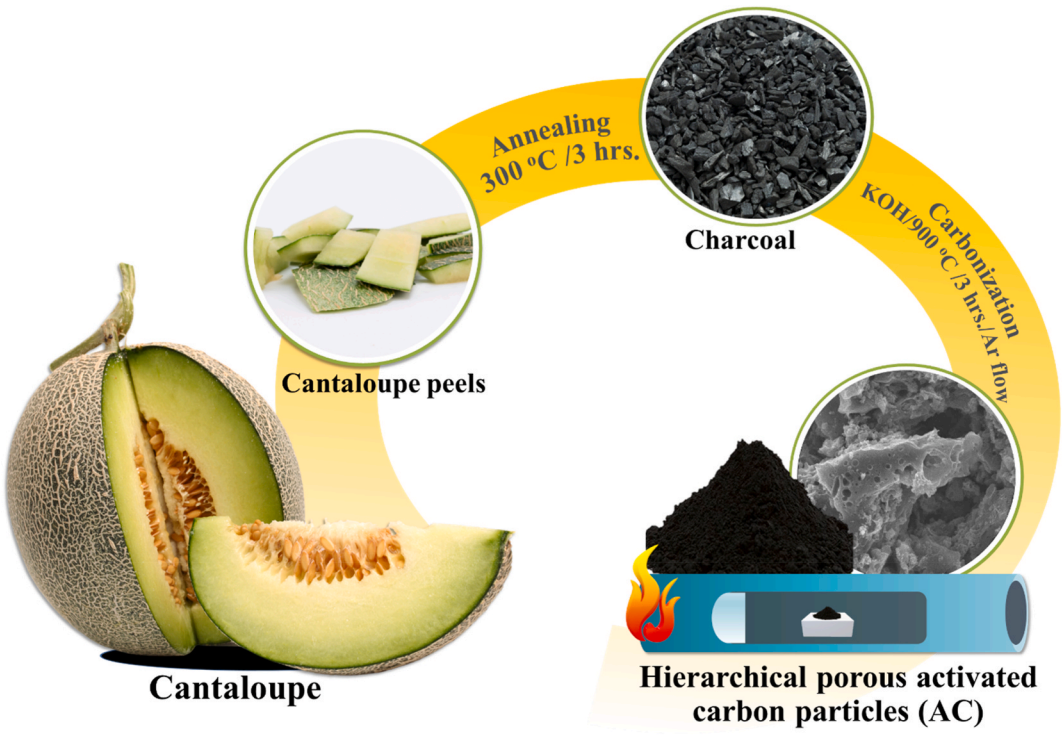

Scheme 1. Preparation of hierarchical porous activated carbon particles.

2. Materials and methods

2.1. Materials

Cantaloupe was purchased from a local market. The fly ash powder utilized in the present investigation was obtained from the Mae Moh Power Plant in the northern Thai province of Lampang. PEDOT:PSS, titanium tetrachloride ($TiCl_4$), tetraammineplatinum (II) chloride hydrate (Pt $(NH_3)_4Cl_2{\cdot}xH_2O$), ethyl cellulose ($C_{20}H_{38}O_{11}$), isopropyl alcohol (>99.8 %, C_3H_8O), tert-butanol (>99.70 %, $C_4H_{10}O$), 1-propyl-3-methylimidazolium iodide (>98 %, $C_{16}H_{31}IN_2$), lithium carbonate (99.99 %, Li_2CO_3), tert-butylpyridine (96 %, $C_{13}H_{21}N$), and acetonitrile (99.8 %, CH_3CN) were obtained from Sigma-Aldrich. Ruthenizer 535-bisTBA and PST-18NR paste were acquired from Solaronix S.A. Lithium iodide anhydrous (99.99 %, Lil) and lithium perchlorate anhydrous (99 %, $LiClO_4$) were obtained from Alfa Aesar. Iodine (>99.8 %, I_2) was acquired from Riedel-de Haen. Fluorine-doped tin oxide glass (FTO, 15 Ω/sq) was obtained from Solaronix. All chemicals were used as received with no further purification.

2.2. Preparation of the AC powder

The cantaloupe peels were washed, chopped into small pieces, rinsed with water, and dried in the sun for 12 h. The dried cantaloupe peels were then annealed at 300 °C for 3 h in an air atmosphere to produce charcoal. The hierarchical porous activated carbon generated from cantaloupe peels was produced by grinding charcoal briquettes with KOH in a 1:1 mass ratio and then carbonizing the resulting material at 900 °C for 3 h with a heating rate of 10 °C/min under an argon atmosphere, as shown in Scheme 1.

2.3. Preparation of the AC:FA CEs

Before use, the fly ash powder was heated to 80 °C and held at that temperature for 24 h. The obtained AC was mixed in various ratios with fly ash, 1:3, 1:1, and 3:1 (wt./wt.). These samples are referred as AC:FA-(1:3), AC:FA-(1:1), and AC:FA-(3:1), respectively. Dispersed AC:FA powder was then added to 500 μL of PEDOT:PSS as binder with 500 μL of distilled water and stirred for 10 min. AC:FA pastes were coated onto clean FTO glass using a doctor blade method, as previously reported [30]. Finally, the obtained AC:FA CEs were annealed at 80 °C for 6 h, as shown in Scheme 2. Then, 3 mM of tetraammineplatinum (II) chloride hydrate and 0.2 g of ethyl cellulose in isopropyl alcohol were used to produce Pt CEs, which were spin-coated at 500 rpm and 1500 rpm for 30 s and dried at 80 °C on clean FTO glass for three cycles before being sintered at 500 °C for 1 h under atmospheric air.

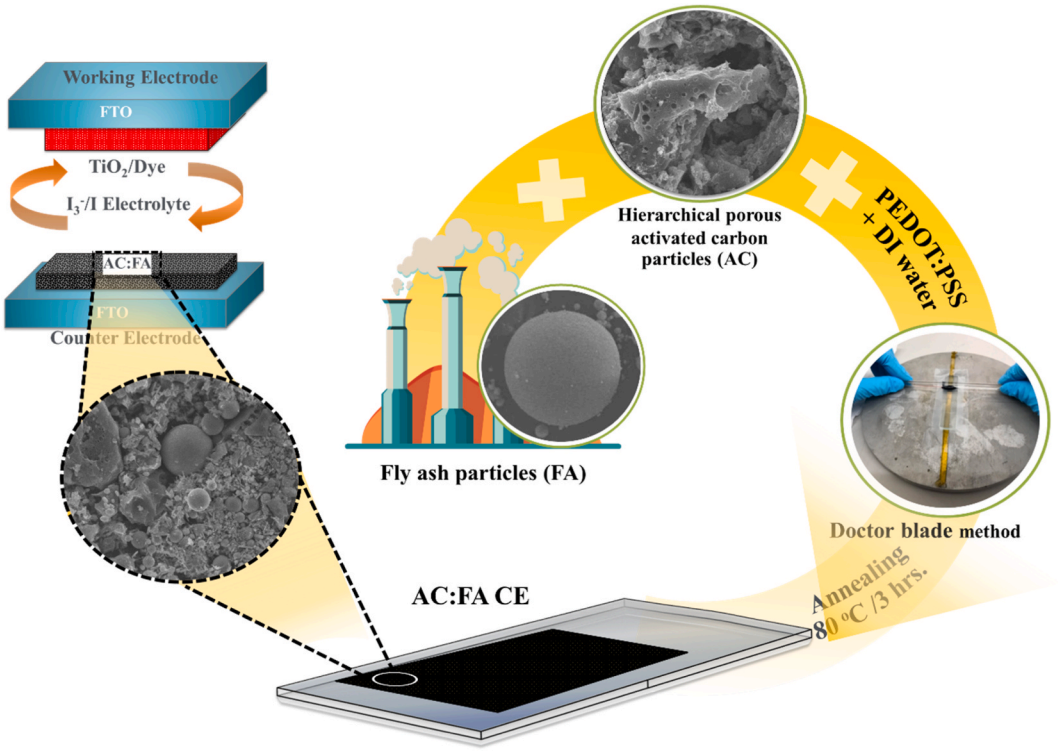

Scheme 2. Preparation of AC:FA counter electrodes and DSSC structure.

2.4. Fabrication of DSSCs

PST-18NR paste was screen-printed onto an FTO substrate to produce working electrodes (WEs) with an active photoanode area of 0.25 square centimeters. Clean FTO glass pieces were initially coated with a 40 mM of aqueous titanium tetrachloride solution by chemical bath deposition and subsequently heat-treated at 70 °C for 30 min to form a blocking layer. A TiO_2 layer was also prepared using a screen method with 18NR-T paste, seven times (thickness about 16–18 μm), on the blocking layer. Then, the prepared film was heated at 500 °C for 60 min under an air atmosphere. After that, the WEs were immersed in a 0.5 mM of N719 dye for 24 h, prepared using 0.5 mM of ruthenizer 535-bisTBA and 50 ml of tert-butanol in 50 ml of acetonitrile [31].

Previous studies used an I^-/I_3^- electrolyte for DSSC preparation [32], employing 0.1 M lithium iodide anhydrous, 0.05 M iodine, 0.6 M 1-propyl-3-methylimidazolium iodide, 2.5 mM lithium carbonate and 0.5 M tert-butylpyridine in acetonitrile. Parafilm was used as a separator for the DSSC asymmetrical cell structure along with a drop of I^-/I_3^- electrolyte, in a semi-closed approach. To perform EIS and Tafel tests on the CE catalysts, two FA CEs with active areas of 0.5 cm^2 were joined in CE:CE symmetric cells (shown in Scheme 2) using a parafilm separator. The cells were then filled with I^-/I_3^- electrolyte.

2.5. Characterization

The crystal structure, chemical functional groups and morphology of AC:FA films were examined using X-ray diffractometry (XRD) (Bruker D8 Advance with Cu-Kα source), Fourier transform infrared spectroscopy (FT-IR, Bruker UV-1900) and scanning electron microscopy (SEM, LEO-1450 V P, UK), respectively. A nitrogen adsorption-desorption isotherm was employed to determine the specific surface area and pore volume using the Brunauer-Emmett-Teller (BET) and Barrett-Joyner-Halenda (BJH) techniques, respectively. To evaluate the electrocatalytic activity of the AC:FA CEs, the counter electrode's catalytic activity was assessed in a three-compartment cell using cyclic voltammetry (CV; Gamry REF 3000, U.S.A.) at a scan rate of 20 mV/s. The reference electrode was Ag/AgCl, while the counter electrode was a Pt plate. The three-electrode system's CV electrolyte was made using 10 mM of lithium iodide anhydrous, 1 mM of iodine and 0.1 M of lithium perchlorate anhydrous in acetonitrile.

Electrochemical impedance spectroscopy (EIS) was performed on a DSSC asymmetrical cell and a CE:CE symmetrical cell with frequencies ranging from 0.2 Hz to 100,000 Hz and an alternating current amplitude of 10 mV under solar light illumination intensity of 100 $mWcm^{-2}$ and dark conditions, respectively. The observed impedance spectra were matched with the program, Gamry Echem Analyst, using an equivalent circuit model.

In the dark, CE:CE asymmetrical cells with identical electrolyte and measurement conditions as the symmetric CE:CE symmetrical cell impedance test were found to exhibit Tafel polarization. A solar simulator (Peccell, PE-L111, Japan) system with a light intensity of 100 mW cm^{-2} was utilized to examine the performance of these solar cells.

3. Results and discussion

3.1. Crystal structure, chemical functional groups and morphological analysis

The crystal structures of the AC, FA, and AC:FA-(3:1) film were determined using XRD analysis. These results are presented in Fig. 1. The crystalline phases of mullite ($Al_6Si_2O_{13}$), quartz (SiO_2), lime (CaO) and hematite (Fe_2O_3) are shown in Fig. 1(a) in the XRD pattern of FA [16,33]. As seen in Fig. 1(b), raw AC displayed two broad diffraction peaks at 2θ values of approximately 27.54° and 42.68°. These peaks corresponded to the (002) and (110) planes of a material with the amorphous nature of graphite [12]. In the instance of the AC:FA-(3:1) film (Fig. 1(c)), the XRD pattern shows that after mixing with AC, the peak intensity of the FA appears at a 2θ angle of approximately 29.23°. This indicates that FA can intercalate in AC crystals. Additionally, it has been demonstrated that FA and AC may

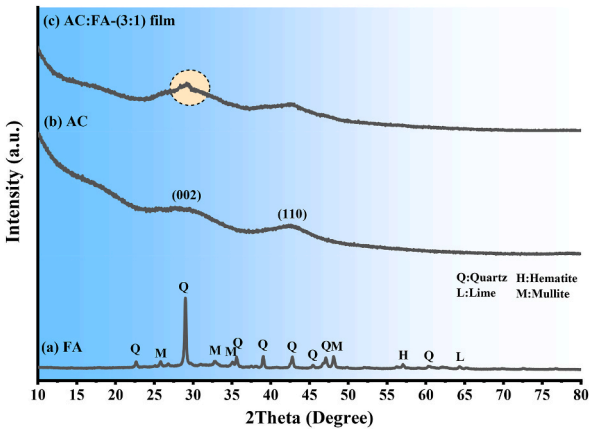

Fig. 1. XRD pattern of AC (a), FA (b), and AC:FA-(3:1) films (c).

intramolecularly interact with one another. However, the PEDOT:PSS binder was not detected, possibly because its level was below the XRD detection limit.

AC and FA powders, as well as the AC:FA film's chemical functional groups were identified *via* FTIR analysis. FT-IR spectra of the AC powder are shown in Fig. 2(a). Due to the vibration of water molecules, the wide peak at 3432 cm^{-1} corresponds to the bands of the O–H groups. The presence of aliphatic C–H stretching is responsible for the apparent peaks at 2930 and 2850 cm^{-1} [34]. The presence of C═C groups causes an observed peak at 2352 cm^{-1}. C═N stretching vibrations are responsible for the peak at 2082 cm^{-1}. The peak at 1625 cm^{-1} may possibly be related to the stretching of carboxylic acids by C═O bonds or C═C bonds as well as by phenolic hydroxyls [35]. Asymmetric and symmetric C–H bending vibrations are ascribed to the 1435 cm^{-1} band. Stretching vibrations of C–H are associated with the weak band at 875 cm^{-1} [36]. In the instance of FA, silica's antisymmetric Si–*O*–Si stretching mode is associated with a band at 1100 cm^{-1}, whereas Si–*O*–Al stretching was identified at 605 cm^{-1} [37], as shown in Fig. 2(b). After compositing, as shown in Fig. 2(c), absorption peaks at 3432, 2930, 2850, 1625, 1435 and 1100 cm^{-1} appeared faintly in the AC:FA-(3:1) film, suggesting the possibility of intermolecular interactions among the component materials. Furthermore, the SO_3H group of PSS and the C–S bonds in the thiophene rings of PEDOT both exhibit stretching vibrations of the PEDOT:PSS binder, which are responsible for the wide absorption peaks at around 785 to 1300 cm^{-1}, respectively [16].

The possible mechanism of chemical bonding in an AC:FA CE can be attributed to different types of interactions, as indicated in Scheme 3. They are (i) physical interactions of FA that can occur between FA particles and the AC surface, as well as between FA and the PEDOT:PSS polymer. This is due to van der Waals forces, which are important in particle-particle adhesion, especially when the particles are close [38,39], and (ii) chemical bonding can contribute to particle-particle adhesion between FA and FA particles as well as between FA and AC. This may occur as a result of hydrogen bonding interactions between hydroxyl groups on particle surfaces. Furthermore, PEDOT:PSS may attach to the surfaces of AC or FA particles and act as a binder to attach the particles to the FTO substrate and connect them *via* hydrogen bonding between the OH groups on particle surfaces and SO_3H of the PSS structure [16]. PEDOT:PSS is formed based on the ionic bonds between the SO_3^- groups of PSS and the thiophene rings of PEDOT [40–42].

The morphologies of the AC, FA, and AC:FA films are shown in Fig. 3. SEM images of the AC films are shown in Fig. 3(a and a-1). The AC particles clearly have a highly porous surface with a complex structure made of linked pores forming a three-dimensional network of pores of different sizes and shapes. The pores range from micro-to mesopores, which provide for an AC film with high surface area. The distribution of fly ash particles, both spherical and amorphous, with diameters ranging from a few micrometers to 20 μm, is seen in the SEM images of the FA film in Fig. 3(b and b-1). In Fig. 3(c and c-1), the film surfaces are rougher for the composite than the surfaces of the AC and FA films. This is due to a combination of different shaped particles, resulting in a composite film with a high specific surface area that promotes diffusion of electrolyte ions and redox reactions.

3.2. Surface area and porosity

An N_2 adsorption-desorption technique was used to assess the surface area and porous characteristics of AC samples. It was found that the N_2 adsorption-desorption isotherm has typical II Type behavior with an H4 hysteresis loop, as illustrated in Fig. 4. According to measurements of the BET surface area and total pore volume of AC, 1958.07 $m^2\ g^{-1}$ and 1.18 $cm^3\ g^{-1}$, respectively, KOH activation appears to be a useful technique for boosting the material's specific surface area as well as increasing its porosity. The BJH pore size distribution curve (inset Fig. 4) was used to calculate the porosity of the AC. The pore size distribution, ranging from 1.2 to 2 nm and 2–5 nm, indicates that AC has both mesoporous and microporous characteristics.

Using Scheme 4, it is possible to describe the mechanism of porosity formation on the surface of as-prepared AC by KOH activation and carbonization. These results imply that larger micro- and mesopores were produced when KOH reacted with a substantial amount of the carbon (C) species in charcoal. Several chemical processes took place during the KOH activation to produce hierarchical porous AC samples. When the pyrolysis temperature was increased to over 700 °C, KOH that had penetrated the charcoal's structure melted to form potassium alkaline compounds such potassium carbonate (K_2CO_3), potassium oxide (K_2O), and potassium (K) and then interacted

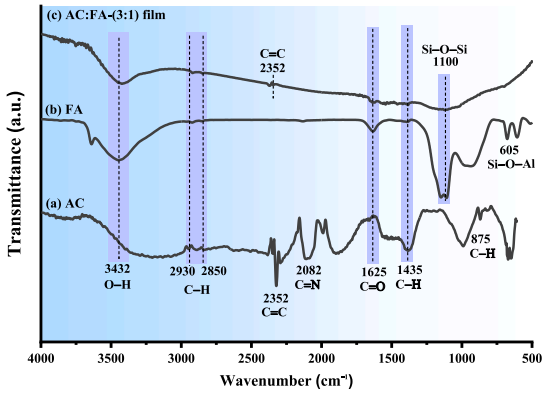

Fig. 2. FTIR pattern of AC powder (a), FA powder (b), and AC:FA-(3:1) films (c).

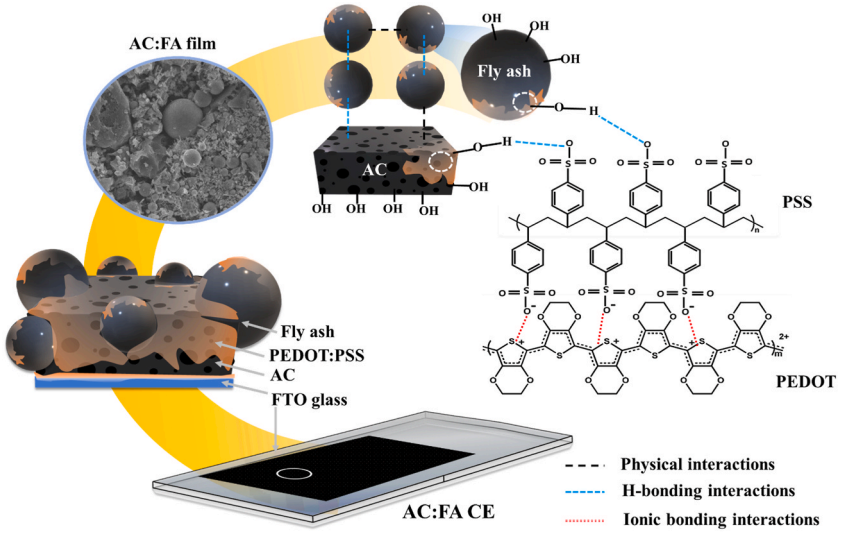

Scheme 3. Possible mechanism of chemical bonding of AC:FA CE.

with the carbon according to Eqs. (1)–(5)). Carbon monoxide (CO), carbon dioxide (CO_2), and other formed gases spread out through the pores, increasing the number of micro- and mesopores on the surface of AC as a result of a reaction between the intermediates, K_2CO_3, K_2O, and K with the C species of charcoal [43–45].

$$6KOH + 2C \rightarrow 2K + 3H_2 + 2K_2CO_3 \quad (1)$$

$$K_2CO_3 + C \rightarrow K_2O + 2CO \quad (2)$$

$$K_2O + C \rightarrow 2K + CO \quad (3)$$

$$K_2CO_3 \rightarrow K_2O + CO_2 \quad (4)$$

$$2K + CO_2 \rightarrow K_2O + CO \quad (5)$$

3.3. Electrocatalytic activity

Cyclic voltammetry was used to assess the electrocatalytic activity of as-prepared CEs towards the I^-/I_3^- redox pair. The CV curves of several CEs utilizing a three-electrode technique are shown in Fig. 5(a). The two pairs of I^-/I_3^- redox peaks were seen on the FA, AC, and FA:AC composite samples. These are depicted on the CV curves of Fig. 5(b). In these CV curves, the cathodic peaks (negative region) are related to the reduction reaction of I_3^- (Eq. (6)), while the anodic peaks (positive region) result from the oxidation process of I^- and I_3^- (Eq. (7)) [46]. In Fig. 5(c), the Pt sample displays two pairs of redox peaks during reduction (Eq. (6) and (8)) and oxidation (Eq. (7) and (9) [47].

$$I_3^- + 2e^- \rightarrow 3I^- \quad (6)$$

$$3I^- - 2e^- \rightarrow I_3^- \quad (7)$$

$$3I^- + 2e^- \rightarrow 2I_3^- \quad (8)$$

$$2I_3^- - 2e^- \rightarrow 3I_2 \quad (9)$$

In a DSSC, the peak to peak difference of potential (E_{pp}), and cathodic peak current density (J_{pc}) can be used to analyze the redox reaction of I^-/I_3^-. A superior electrochemical catalyst is indicated by a higher current density toward the cathodic side and a lower E_{pp} value [48]. Greater J_{pc} values were seen by increasing the amount of AC in the FA (Fig. 5(b)). This is due to a larger surface area within the hierarchical porous structure of AC. The relative electrochemical results are presented in Table 1. The J_{pc} value of the AC:FA-(3:1) CE was enhanced to 0.13 mA cm^{-2} by addition of an optimal the amount of AC. This suggests that compared to the FA sample, AC:FA composite samples have a stronger redox reaction and more electrolyte mobility inside the hierarchical porous structure of AC.

Furthermore, the J_{pc} value of AC:FA CEs is higher than the Pt CE (0.47 mA cm^{-2}), which may be due to the double-layer capacitance behavior of AC arising from a more porous structure with a high specific surface area. This can provide a higher contact potential between the electrode material and the electrolyte than a Pt CE [49] (seen in Fig. 5(c)). However, due to its strong electrical

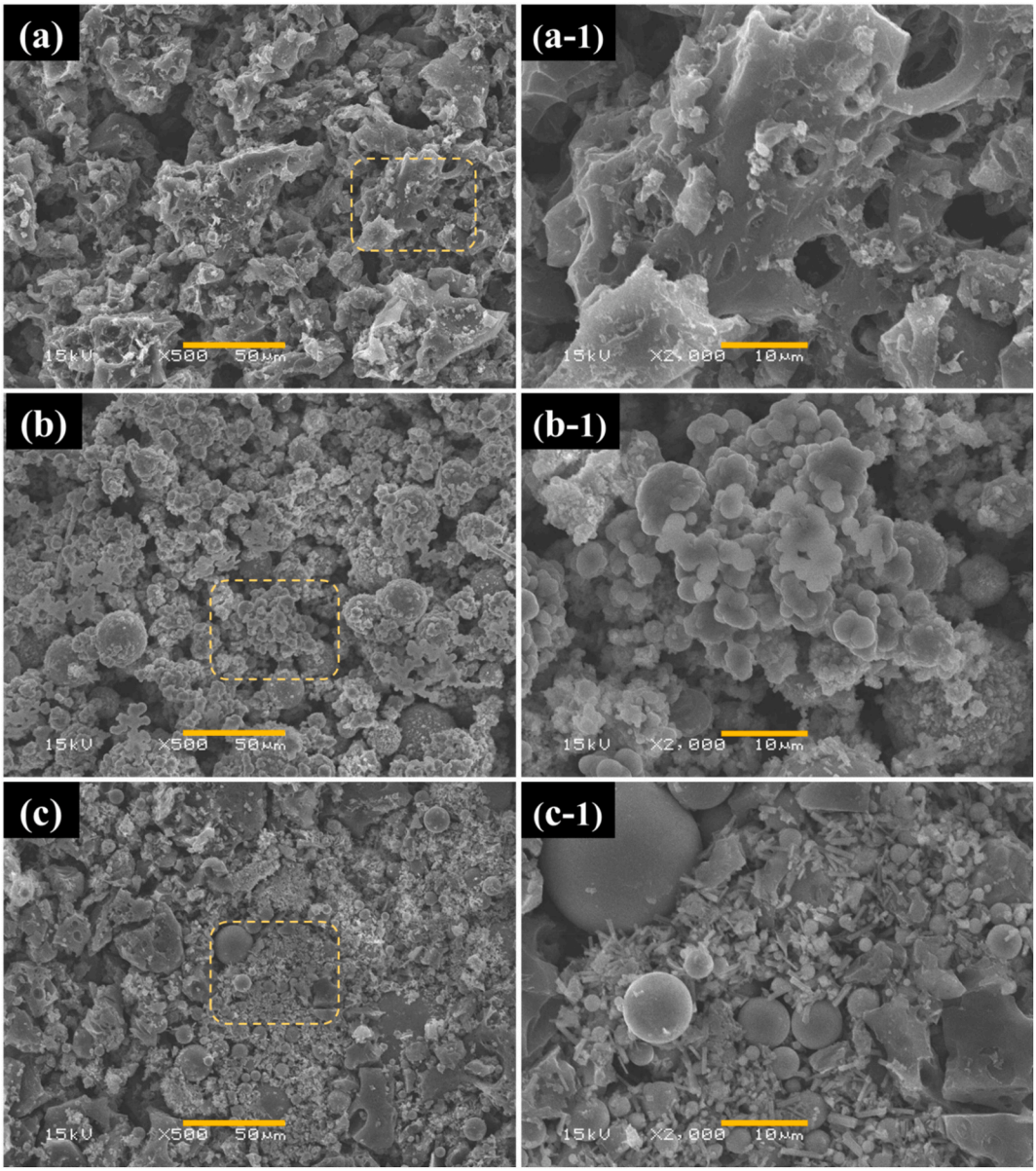

Fig. 3. SEM images of AC (a and a-1), fly ash (b and b-1), and AC:FA-(3:1) films (c and c1).

conductivity and charge carrier capabilities, the E_{pp} value (0.26 V) of the Pt CE is lower than that of other CEs (0.47–0.84 V), suggesting a fast oxidation-reduction process. These results are similar to those of Riaz et al., who created composites of activated charcoal and reduced graphene sheets as CEs (GO:AC). The GO:AC electrode's J_{pc} value was significantly larger than that of a Pt electrode. This higher J_{pc} value is due to the electrode's high surface area and promotion of its catalytic process [48]. Additionally, Sun *et al.* produced CEs using graphite nanoplatelets attached to an exfoliated activated carbon filler (GnP/AC). This result demonstrates the high J_{pc} value of a GnP/AC (-3.89 mA cm^{-2}) composite in comparison to Pt (-2.88 mA cm^{-2}) [50].

The charge transfer resistance and electrochemical catalytic activity for various CEs were also evaluated using EIS. The equivalent circuit of the DSSC asymmetric and CE-CE symmetric cells are shown in Scheme 5. In a DSSC asymmetric cell (Scheme 5(a)), the series resistance, which comprises the sheet resistance of the FTO glass and the cell's contact resistance, is designated as R_S. The charge-transfer resistance and double-layer capacitance at the exposed FTO/electrolyte interface are denoted as R_{FTO} and C_{FTO}, respectively. The charge-transfer resistance of the charge recombination process of electrons in the TiO_2 film and I_3^- ions in electrolyte is represented by r_{ct}. Chemical capacitance of the TiO_2 film is denoted by $C\mu$. The transport resistance of the electrons in the TiO_2 film is r_t, and the resistance and capacitance at the FTO/TiO_2 contact are denoted as R_{CO} and C_{CO}, respectively. These parameters can be reduced to R_S connected with the resistance and capacitance at the TiO_2-dye/electrolyte interface (R_{WE} and C_{WE}). This is because all the

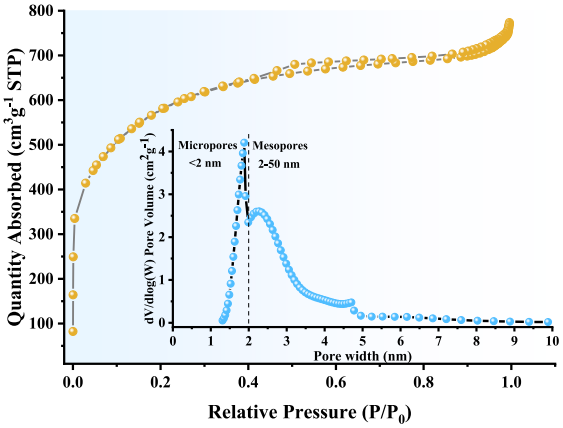

Fig. 4. N_2 adsorption-desorption isotherm of AC powder; the inset shows a pore size distribution curve.

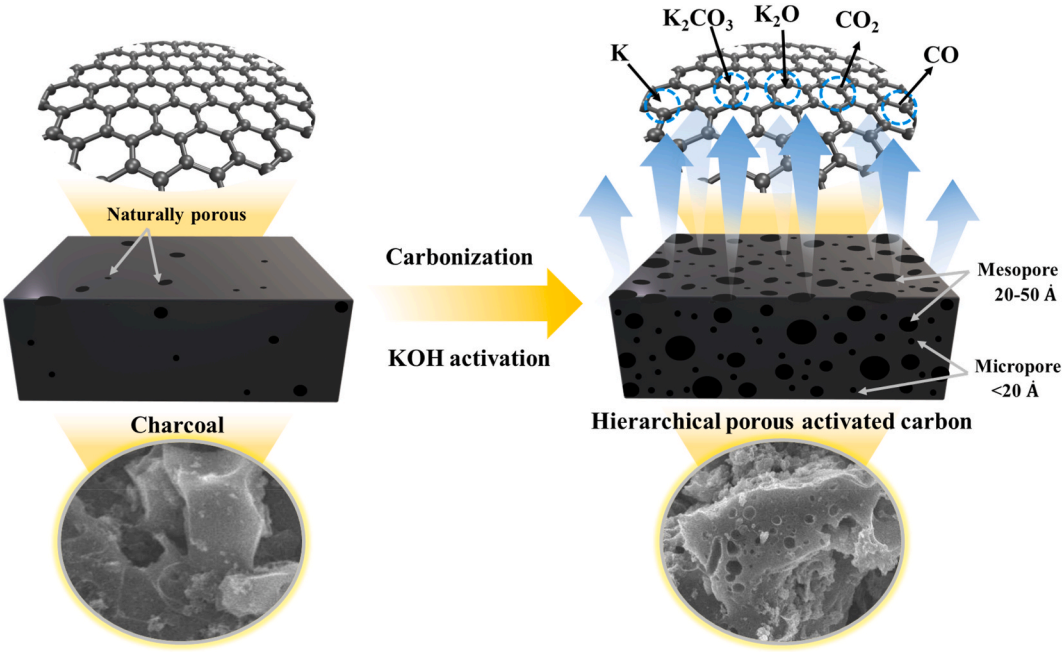

Scheme 4. Mechanism of porosity generation on AC surfaces.

components combine and present only one semicircular arc in the medium-frequency range (the second semicircle). Thus, it is difficult to determine the effect each component from a single semicircular arc. The charge-transfer resistance and double-layer capacitance at the CE/electrolyte interface in a DSSC asymmetric cell are denoted as R_{CE} and C_{CE}, respectively, which is the semicircular arc in the high-frequency range (the first semicircle). The Warburg element (Z_D) is used to demonstrate the Nernst diffusion of I_3^- in the electrolyte in the low frequency region [51,52].

In the instance of the CE-CE symmetric cell (see Scheme 5(b)), R_{S1}, R_{CE1}, and C_{CE1} represent the series resistance including the sheet resistance of the FTO glass and the contact resistance of the cell in a CE-CE symmetric cell, the charge transfer resistance at the CE/electrolyte interface, and the related double-layer capacitance at the CE/electrolyte interface, respectively [50,53–55]. Since the electrodes are identical, the charge transfer resistance and double-layer capacitance can combine and show only one arc as the first semicircle (high frequency region). The total R_{CE1} value is double the R_{CE1} value and the total CPE_{CE1} value is half the CPE_{CE1} value. This is because summation is in series with the same parallel RC. The Nernst diffusion (Z_D) of I_3^- in the electrolyte is present in the low frequency region. These values were identified by fitting Nyquist plots with an equivalent circuit in Gamry Echem Analyst software, as illustrated in Fig. 6 with results listed in Table 1.

The sum of the impedance of Ohmic series resistance (Z_S), the charge transfer resistance at the counter electrode (Z_{CE}), the charge

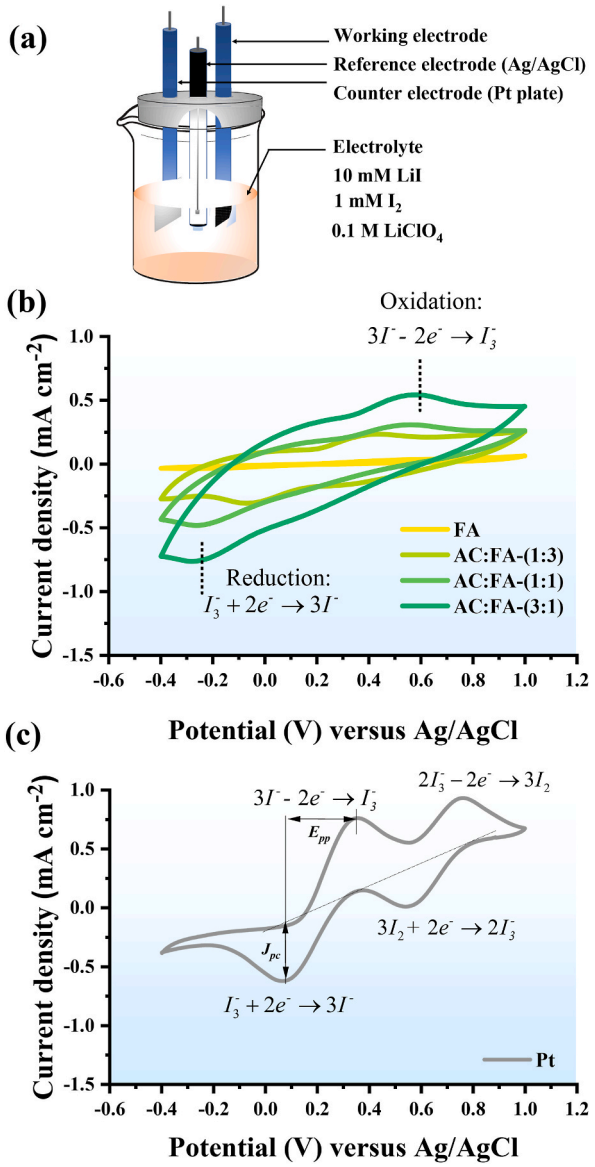

Fig. 5. Schematic of a three-compartment CV (a), CV curves of FA and AC:FA with different proportions (b) and Pt CEs (c).

Table 1
Summary of the electrocatalytic and electrochemical characteristics of the fabricated samples, including the peak to peak voltage separation (E_{pp}), cathodic peak current density (J_{pc}), diffusion-limited current density ($J_{\lim}$), and exchange current density (J_0).

Counter electrode	J_{pc} (mA cm^{-2})	$J_{\lim}$ (mA cm^{-2})	J_0 (mA cm^{-2})	CE-CE cells		DSSC cells		
				R_{S1} (Ω cm^2)	R_{CE1} (Ω cm^2)	R_S (Ω cm^2)	R_{CE} (Ω cm^2)	R_{WE} (Ω cm^2)
FA	0.01	0.45	0.07	10.85	176.65	11.65	12.06	90.95
AC:FA-(1:3)	0.06	2.62	0.52	9.05	36.81	10.75	10.43	37.01
AC:FA-(1:1)	0.09	3.70	0.76	8.63	26.93	10.94	2.95	29.47
AC:FA-(3:1)	0.13	3.91	0.88	9.53	12.20	10.84	2.91	17.39
Pt	0.47	5.89	1.08	8.18	8.85	10.66	2.37	9.63

transfer resistance at the working electrode (Z_{WE}), and the I_3^- diffusion (Z_D) were observed to assess the impedance of dye-sensitized solar cells (DSSCs). It was calculated as:

$$Z_{DSSC} = Z_S + Z_{CE} + Z_{WE} + Z_D \tag{10}$$

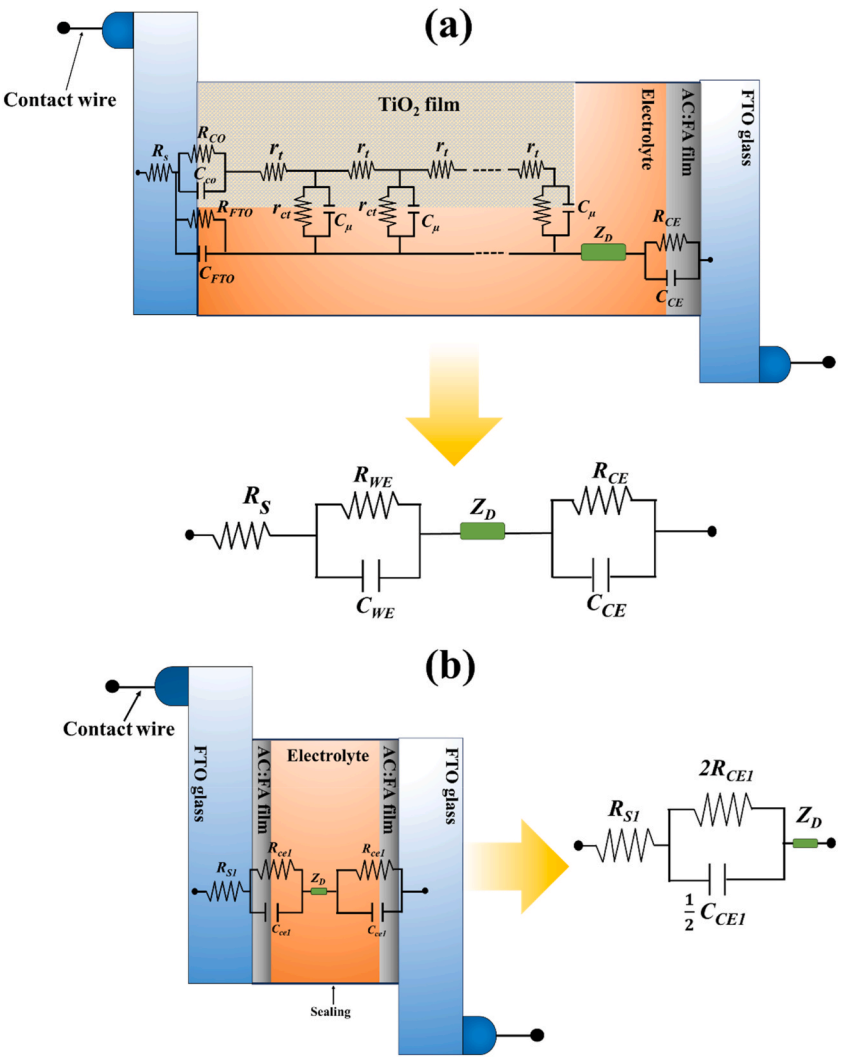

Scheme 5. Equivalent circuit models, which are simplified forms of the basic transmission line model, can potentially be utilized to fit the experimental EIS spectra of asymmetric DSSCs (a) and CE-CE symmetric cells (b).

Z_S is a combination of the series resistance (R_s), which includes the FTO glass sheet resistance and the cell's contact resistance, the resistance at the FTO/TiO_2 contact (R_{CO}), the charge-transfer resistance at CE (R_{CE}), the resistance of the redox mediator (R_D) and the electron transport resistance in the TiO_2 film is R_t ($R_t = r_t/L$) where L is the thickness of the mesoscopic TiO_2 film [31,51].

$$Z_S = R_{S,total} = R_s + R_{CO} + R_{CE} + \frac{1}{3}R_t + R_D \tag{11}$$

Generally, the sheet resistance of FTO glass significantly contributes to series resistance, and it might be reduced with improved sample design. Additionally, R_D may be decreased by increasing the conductivity of the electrolyte and bringing the counter electrode closer to the TiO_2 layer, so that R_{CE} may be decreased by increasing the porosity of the deposited material at the counter electrode [51].

The charge transfer mechanism at the interface of the counter electrode and electrolyte is represented by the first arc at high frequencies (Fig. 6(a)). This may be characterized as an *R–C* parallel circuit and expressed in terms of a constant phase element (*CPE*) as follows:

$$Z_{CE} = \frac{R_{CE}}{1 + (j\omega)^{\alpha} R_{CE} C_{CE}} \tag{12}$$

where $j = \sqrt{-1}$ is an imaginary number, $\omega = 2\pi f$ is angular frequency (f is frequency), α is an exponent equal to 1 for a capacitor and is less than 1 for a constant phase element.

A semiconductor couple with carrier recombination at the semiconductor/electrolyte interface (Z_{WE}) is illustrated by the second arc

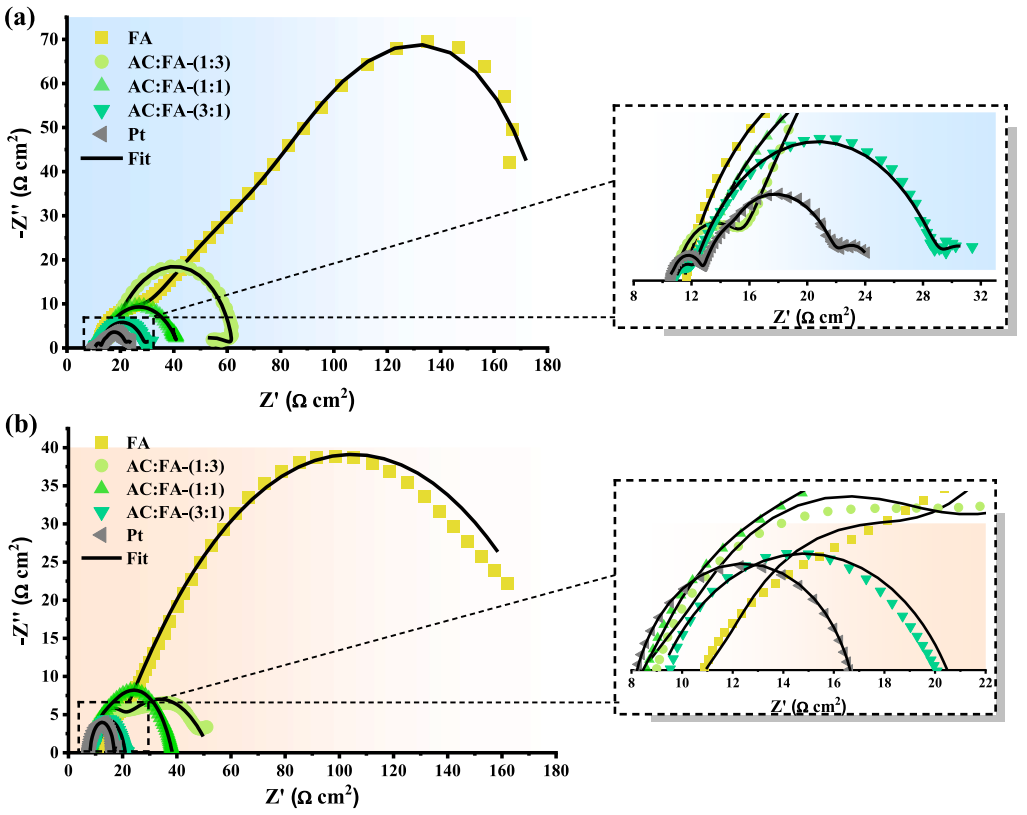

Fig. 6. Nyquist plots of fabricated DSSC cells (a) and CE-CE cell assembly plots (b). Insets display enlarged Nyquist plots.

at intermediate frequencies in Fig. 6(a). EIS is often done using a DSSC's open circuit voltage (V_{oc}) to examine electron transport and recombination. The impedance at the working electrode's interface is given as [56]:

$$Z_{WE} = \sqrt{\frac{R_d R_k}{(1+(j\omega)^{\alpha} R_k Q_k)}} \times \coth\sqrt{\left(\frac{R_d}{R_k}\right)((1+(j\omega)^{\alpha} R_k Q_k)} \tag{13}$$

The diffusion resistance, the electron recombination resistance, and the *CPE* prefactor (in accordance with the chemical capacitance (C_{CE}) of a semiconductor film) are denoted as R_d, R_k, and Q_k, respectively. This R–C parallel circuit may be described to express the charge transfer mechanism at the working electrode in a simpler form:

$$Z_{WE} = \frac{R_{WE}}{1+(j\omega)^{\alpha} R_{WE} C_{WE}} \tag{14}$$

According to Fig. 6(a) and (b), the diffusion impedance of I_3^- (Z_D) is the source of the third arc at low frequencies. In comparison to I_3^-, the I^- is present in the redox mediator at very high concentrations. Since diffusion impedance occurs just in the low-frequency region, only I_3^- addresses it [56,57]. The following equation gives the finite-length Warburg impedance for I_3^- diffusion impedance:

$$Z_D = R_D \sqrt{\frac{D/L^2}{j\omega}} \tanh\sqrt{\frac{j\omega}{D/L^2}} \tag{15}$$

where R_D, D, and L represent the diffusion resistance, triiodide diffusion coefficient, and effective thickness, which is the electrolyte film's half-thickness, respectively. As a result, Eq. (10) may be expressed in terms of resistances as:

$$Z_{DSSC} = R_S + \frac{R_{CE}}{1+(j\omega)^{\alpha} R_{CE} C_{CE}} + \frac{R_{WE}}{1+(j\omega)^{\alpha} R_{WE} C_{WE}} + R_D \sqrt{\frac{D/L^2}{j\omega}} \tanh\sqrt{\frac{j\omega}{D/L^2}} \tag{16}$$

For CE-CE symmetry, impedance is calculated using:

$$Z_{CE-CE} = R_S + \frac{2R_{CE1}}{1 + (j\omega)^{\alpha} R_{CE1} C_{CE1}} + R_D \sqrt{\frac{D/L^2}{j\omega}} \tanh \sqrt{\frac{j\omega}{D/L^2}} \quad (17)$$

From the Nyquist spectra of the DSSC asymmetric cell shown in Fig. 6(a) and their corresponding values in Table 1, a pure FA CE has the largest R_{CE} and R_{WE} values, 12.06 and 90.95 Ω cm^2. This suggests that FA CE's charge transfer at the CE/electrolyte and WE/electrolyte interfaces are poor. The R_{CE} and R_{WE} values rapidly decrease when AC is incorporated into the FA film, showing increased electrocatalytic activity and charge transfer [55,58]. Compared to the AC:FA-(1:3) CE (R_{CE} and R_{WE} of 10.43 and 37.01 Ω cm^2) and the AC:FA-(1:1) CE (R_{CE} and R_{WE} of 2.95 and 29.47 Ω cm^2), the AC:FA-(3:1) CE's R_{CE} and R_{WE} values are lower, 2.91 and 17.39 Ω cm^2, respectively. Although the AC:FA-(3:1) CE has low R_{CE} and R_{WE} values, it nevertheless has larger R_{CE} and R_{WE} values than a Pt CE (2.37 and 9.63 Ω cm^2, respectively). This is due to the Pt CE's strong charge transfer and catalytic activity.

According to the Nyquist spectra of CE-CE symmetric cells shown in Fig. 6(b), the R_{CE1} trend was similar to that of R_{WE} and R_{CE}, with the R_{CE1} tending to decrease with introduction of AC into the FA film. The AC:FA-(3:1) CE had a lower R_{CE1}, 12.20 Ω cm^2, indicating a stronger electron transfer mechanism [58], compared to the pure FA CE (176.65 Ω cm^2), AC:FA-(1:3) CE (36.81 Ω cm^2), and AC:FA-(1:1) CE (26.93 Ω cm^2), while the R_{CE1} value of the Pt CE was 8.85 Ω cm^2. The lower R_{CE1} value of the Pt CE can be ascribed to greater charge transfer at the CE/electrolyte interfaces. Furthermore, the R_S and R_{S1} values of the tested counter electrode were found to range from 10.27 to 11.65 Ω cm^2 and 8.18–10.85 Ω cm^2, respectively. These values suggest excellent bonding between the catalyst layer and the FTO substrate [55]. The lower R_S value results in an increased *FF* value leading to an improved DSSC efficiency [51].

Tafel polarization measurements were performed in a CE-CE symmetric cell assembly with an I^-/I_3^- electrolyte, as illustrated in Fig. 7. This was done to further examine the catalytic properties of the as-prepared CEs. The exchange current density in the Tafel zone is J_o, which is the point where the tangent to the cathodic branch intersects the equilibrium (zero) potential ordinate. J_o is inversely proportional to R_{CE1}:

$$J_0 = \frac{RT}{nFR_{CE1}} \quad (18)$$

where R_{CE1} is the charge transfer resistance at the CE/electrolyte interface, T is the absolute temperature, n is the number of electrons engaged in the reduction of I_3^- at the electrode, F is the Faraday constant, and R is the gas constant. Higher J_o values correspond to lower R_{CE1} levels in CE-CE symmetric cells [59,60]. Another important parameter that could be identified from this Tafel curve, depicted in Eq. (19), is the limiting diffusion current density (J_{lim}), which is the intersection of the cathodic branch and the y-axis.

$$J_{\text{lim}} = \frac{2nDCF}{l} \quad (19)$$

where D is the diffusion coefficient, C is the concentration of I_3^- and l is the spacer thickness [60]. Table 1 shows the obtained J_0 and J_{lim} values. Compared to the FA CE (0.07 and 0.45 mA cm^{-2}), the AC:FA-(3:1) CE's J_0 and J_{lim} values were 0.88 and 3.91 mA cm^{-2}, respectively. This suggests that the AC:FA-(3:1) CE has a stronger catalytic activity for redox pair regeneration, a higher charge transfer rate at the CE/electrolyte interface, and greater diffusion of I_3^- in the electrolyte [59–61]. However, due to the Pt CE devices' larger J_0 and J_{lim} values, the electrocatalytic activity of the AC:FA-(3:1) CE is lower than that of a Pt CE. These findings correspond well with our CV and EIS analyses.

3.4. Photovoltaic performance of a DSSC based on the AC:FA CEs

As shown in Fig. 8 and Table 2, the corresponding photovoltaic parameters with standard deviations for the open-circuit voltage (V_{oc}), the short-circuit current densities (J_{sc}), the fill factor (*FF*), and the power conversion efficiency (PCE) based on four cells for the DSSCs with the CEs of FA, AC:FA-(1:3), AC:FA-(1:1), AC:FA-(3:1) and Pt, are presented. The PCE was calculated using Eq. (20) [31,51].

$$\text{PCE} = \frac{J_{sc} \times V_{oc} \times FF}{P_{in}} \times 100\% \quad (20)$$

A DSSC's fill factor may be calculated as:

$$FF = \frac{P_{\text{max}}}{J_{sc} \times V_{oc}} \quad (21)$$

where P_{max} is the maximum output power.

The PCE of the DSSC cells with AC:FA CEs are substantially higher than that with FA CE (3.02 ± 0.17 %). As the content of AC in the composite film increases, the PCE of these DSSCs increases from 5.56 ± 0.46 % (AC:FA-(1:3) CE) to 5.81 ± 0.19 % (AC:FA-(3:1) CE). The significant enhancement in the PCE is due to the high surface area conductivity and catalytic activity created by the porous structure of AC. This provides a higher *FF* and J_{sc} for the solar cells. Higher J_{sc} and *FF* values imply that the counter electrode has better electro-catalytic active area and excellent charge transfer capability [60,62]. The DSSC cell with the AC:FA-(3:1) CE presents the greatest PCE value of all the DSSCs equipped with AC:FA composite CEs, with a V_{oc} of 0.78 ± 0.001 V, J_{sc} of 14.57 ± 0.34 mA cm^{-2}, and FF of 0.51 ± 0.01. According to the CV, Tafel, and EIS studies, the electrocatalytic activities of the CEs have magnitudes in

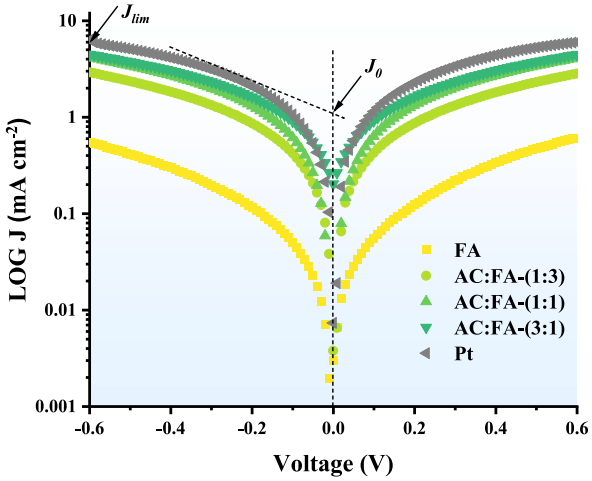

Fig. 7. Tafel plots of CE-CE cells assembled with various CEs.

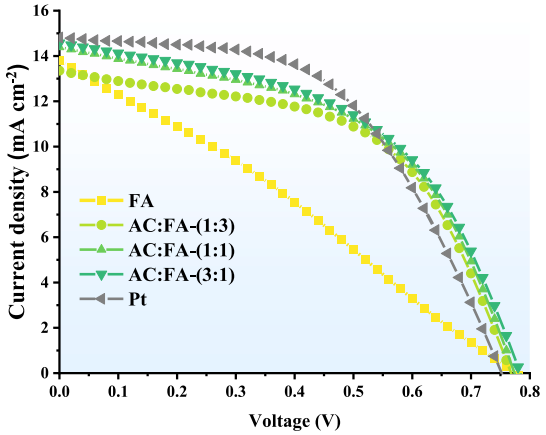

Fig. 8. J-V curves of DSSCs with different CEs at 1.5G AM (100 mW cm^{-2}).

Table 2
Comparison of photovoltaic parameters of DSSCs assembled with various CEs, obtained at a 100 mW cm^{-2} (AM 1.5G) light intensity.

Counter electrode	V_{oc} (V)	J_{sc} (mA cm^{-2})	*FF*	PCE (%)
FA	0.78 ± 0.002	13.82 ± 0.30	0.28 ± 0.01	3.02 ± 0.17
AC:FA-(1:3)	0.77 ± 0.010	13.35 ± 1.26	0.54 ± 0.03	5.56 ± 0.46
AC:FA-(1:1)	0.77 ± 0.001	14.39 ± 1.39	0.52 ± 0.03	5.72 ± 0.25
AC:FA-(3:1)	0.78 ± 0.001	14.57 ± 0.34	0.51 ± 0.01	5.81 ± 0.19
Pt	0.75 ± 0.003	14.81 ± 1.05	0.53 ± 0.01	5.91 ± 0.46

descending order as Pt > AC:FA-(3:1) > AC:FA-(1:1) > AC:FA-(1:3) > FA. This tendency precisely follows the PCE's of their DSSCs. Although the efficacy of the DSSC cell with the AC:FA-(3:1) CE is lower than that with a Pt CE (5.91 ± 0.46 %), its manufacturing costs are less. For this reason, the AC:FA-(3:1) CE is appealing as a potential replacement for expensive Pt CEs.

4. Conclusions

DSSCs using AC:FA composites as CEs were demonstrated. AC:FA composites were created using PEDOT:PSS as a co-catalyst and a binder, while cantaloupe peel-derived AC particles were synthesized using KOH activation. Counter electrodes' electrocatalytic activity, electrochemical, and photovoltaic properties all improved as the level of AC in the composite film increased. The hierarchical porous structure of AC improves the surface area of a composite film, resulting in a greater reduction of I_3^- ions and charge transfer at WE/electrolyte and CE/electrolyte interfaces, as demonstrated by CV, Tafel and EIS results. DSSCs utilizing the AC:FA-(3:1) CE

obtained a PCE of 5.81 % under optimal conditions, which is close to a DSSC based on a Pt CE (5.91 %). The study results showed that an AC:FA-(3:1) CE is a promising material for Pt-free counter electrodes and provides a creative method for utilizing an affordable composite for effective counter electrodes in DSSCs.

Data availability

Data will be made available on request.

CRediT authorship contribution statement

Nattakan Kanjana: Writing – review & editing, Writing – original draft, Methodology, Conceptualization. **Wasan Maiaugree:** Writing – review & editing, Writing – original draft, Validation, Software, Methodology, Investigation, Funding acquisition, Conceptualization. **Tirapat Wechprasit:** Writing – review & editing, Formal analysis. **Anusit Kaewprajak:** Writing – review & editing, Investigation. **Pisist Kumnorkaew:** Writing – review & editing, Investigation. **Poramed Wongjom:** Writing – review & editing. **Yingyot Infahsaeng:** Writing – review & editing.

Declaration of competing interest

The authors declare that they have no known competing financial interests or personal relationships that could have appeared to influence the work reported in this paper.

Acknowledgments

This work was supported by the Thailand Science Research and Innovation Fundamental Fund fiscal year 2024; the Thammasat University Research Fund (No. TUFT 44/2566), Thammasat University, Thailand, Thailand; the Office of the Permanent Secretary, Ministry of Higher Education, Science, Research and Innovation (OPS MHESI), Thailand Science Research and Innovation (TSRI) (No. RGNS 65–109) and the Thammasat University Research Unit in Energy Innovations and Modern Physics (EIMP). We also would like to thank the Rajamangala University of Technology Isan Surin Campus for their partial financial support.

References

[1] B. O'Regan, M. Grätzel, A low-cost, high-efficiency solar cell based on dye-sensitized colloidal TiO_2 films, Nature 353 (1991) 737–740, https://doi.org/10.1038/353737a0.
[2] J. Gong, K. Sumathy, Q. Qiao, Z. Zhou, Review on dye-sensitized solar cells (DSSCs): Advanced techniques and research trends, Renew. Sust. Energ. Rev. 68 (2017) 234–246, https://doi.org/10.1016/j.rser.2016.09.097.
[3] N. Kanjana, W. maiaugree, S. Tontapha, P. Laokul, A. Chingsungnoen, S. Pimanpang, I. Chaiya, S. Daengsakul, V. Amornkitbamrung, Effect of carbonization temperature on the electrocatalytic property and efficiency of dye-sensitized solar cells derived from corncob and sugarcane leaf agricultural residues, Biomass Conv. Bioref. 13 (2023) 8361–8371, https://doi.org/10.1007/s13399-021-02204-3.
[4] R. Sperenza, M. Reina, P. Zaccagnini, A. Pedico, A. Lamberti, Laser-induced graphene as a sustainable counter electrode for DSSC enabling flexible self-powered integrated harvesting and storage device for indoor application, Electrochim. Acta 460 (2023) 142614, https://doi.org/10.1016/j.electacta.2023.142614.
[5] Y.L. Lee, C.L. Chen, L.W. Chong, C.H. Chen, Y.F. Liu, C.F. Chi, A platinum counter electrode with high electrochemical activity and high transparency for dye-sensitized solar cells, Electrochem. Commun. 12 (2010) 1662–1665, https://doi.org/10.1016/j.elecom.2010.09.022.
[6] M. Wu, M. Sun, H. Zhou, J.-Y. Ma, T. Ma, Carbon counter electrodes in dye-sensitized and perovskite solar cells, Adv. Funct. Mater. 30 (2020) 1906451, https://doi.org/10.1002/adfm.201906451.
[7] M. Wu, Y. Lin, H. Guo, W. Li, Y. Wang, X. Lin, Design a novel kind of open-ended carbon sphere for a highly effective counter electrode catalyst in dye-sensitized solar cells, Nano Energy 11 (2015) 540–549, https://doi.org/10.1016/j.nanoen.2014.11.032.
[8] E. Akman, H.S. Karapinar, Electrochemically stable, cost-effective and facile produced selenium@activated carbon composite counter electrodes for dye-sensitized solar cells, Sol. Energy 234 (2022) 368–376, https://doi.org/10.1016/j.solener.2022.02.011.
[9] N. Shahzad Lutfullah, T. Perveen, D. Pugliese, S. Haq, N. Fatima, S.M. Salman, A. Tagliaferro, M.I. Shahzad, Counter electrode materials based on carbon nanotubes for dye-sensitized solar cells, Renew. Sust. Energ. Rev. 159 (2022) 112196, https://doi.org/10.1016/j.rser.2022.112196.
[10] S.V. Kuppu, M. Senthilkumaran, V. Sethuraman, M. Balaji, C. Saravanan, N. Ahmed, S. Mohandoss, Y.R. Lee, J. Anandharaj, T. Stalin, The surfactants mediated electropolymerized poly(aniline) (PANI)-reduced graphene oxide (rGO) composite counter electrode for dye-sensitized solar cell, J. Phys. Chem. Solid. 173 (2023) 111121, https://doi.org/10.1016/j.jpcs.2022.111121.
[11] B. Karuppasamy, B. Shenbagabalakrishnan, V. Gayathri, Liquid-phase exfoliated graphite-nanosheets as counter electrode for enhanced performance of cost-effective DSSCs, J. Solid State Electrochem. 27 (2023) 1001–1009, https://doi.org/10.1007/s10008-023-05377-1.
[12] G. Murugadoss, K.K. Chinnakutti, G. Manibalan, R.K. Manavalan, K. Brindhadevi, A. Pugazhendhi, Cost-effective carbon black-graphite composite with solid-state based CuSCN electrode for dye-sensitized solar cells, Fuel 348 (2023) 128527, https://doi.org/10.1016/j.fuel.2023.128527.
[13] Y. Zhu, H. Guo, H. Zheng, Y. Lin, C. Gao, Q. Han, M. Wu, Choose a reasonable counter electrode catalyst toward a fixed redox couple in dye-sensitized solar cells, Nano Energy 21 (2016) 1–18, https://doi.org/10.1016/j.nanoen.2016.01.001.
[14] G. Dwivedi, G. Munjal, A.N. Bhaskarwar, A. Chaudhary, Dye-sensitized solar cells with polyaniline: a review, Inorg. Chem. Commun. 135 (2022) 109087, https://doi.org/10.1016/j.inoche.2021.109087.
[15] S. Venkatesan, W.H. Lin, T.H. Hsu, H. Teng, Y.L. Lee, Indoor dye-sensitized solar cells with efficiencies surpassing 26% using polymeric counter electrodes, ACS Sustainable Chem. Eng. 10 (2022) 2473–2483, https://doi.org/10.1021/acssuschemeng.1c07626.
[16] N. Kanjana, W. Maiaugree, P. Laokul, I. Chaiya, T. Lunnoo, P. Wongjom, Y. Infahsaeng, B. Thongdang, V. Amornkitbamrung, Fly ash boosted electrocatalytic properties of PEDOT:PSS counter electrodes for the triiodide reduction in dye-sensitized solar cells, Sci. Rep. 13 (2023) 6012, https://doi.org/10.1038/s41598-023-33020-6.
[17] M.S. Motlagh, V. Mottaghitalab, A. Rismanchi, M.R. Chirani, M. Hasanzadeh, Performance modelling of textile solar cell developed by carbon fabric/polypyrrole flexible counter electrode, Int. J. Sustain. Energy 41 (2022) 1106–1126, https://doi.org/10.1080/14786451.2022.2026356.
[18] J. Huo, X. Wang, X. Zhang, L. Zhang, G. Yue, S. Guo, Porous polypyrrole-derived carbon nanotubes as a cathode material for zinc-ion hybrid supercapacitors, J. Energy Storage 73 (2023) 108925, https://doi.org/10.1016/j.est.2023.108925.

[19] P. Mahajan, R. Datt, V. Gupta, S. Arya, Synthesis and characterization of ZnO@WO_3 core/shell nanoparticles as counter electrode for dye-sensitized solar cell, Surface. Interfac. 30 (2022) 101920, https://doi.org/10.1016/j.surfin.2022.101920.

[20] A. Asok, K. Haribabu, Synthesis and performance of polythiophene-iridium oxide composite as counter electrode in dye sensitized solar cell, Curr. Appl. Phys. 49 (2023) 64–69, https://doi.org/10.1016/j.cap.2023.02.019.

[21] K. Gomathi, S. Padmanathan, A.M. Ali, A.T. Rajamanickam, Construction of Ni doped MoO_3 nanostructures and their application as counter electrode in dye-sensitized solar cells, Inorg. Chem. Commun. 135 (2022) 109079, https://doi.org/10.1016/j.inoche.2021.109079.

[22] H. Wang, W. Wei, Y.H. Hu, NiO as an efficient counter electrode catalyst for dye-sensitized solar cells, Top. Catal. 57 (2014) 607–611, https://doi.org/10.1007/s11244-013-0218-8.

[23] M. Wu, Y. Wang, X. Lin, N. Yu, L. Wang, L. Wang, A. Hagfeldt, T. Ma, Economical and effective sulfide catalysts for dye-sensitized solar cells as counter electrodes, Phys. Chem. Chem. Phys. 13 (2011) 19298–19301, https://doi.org/10.1039/C1CP22819F.

[24] M. Hosseinnezhad, M. Ghahari, G. Mobarhan, S. Rouhani, M. Fathi, Towards low cost and green photovoltaic devices: using natural photosensitizers and MoS_2/Graphene oxide composite counter electrodes, Opt. Mater. 139 (2023) 113775, https://doi.org/10.1016/j.optmat.2023.113775.

[25] Y. Areerob, W.C. Oh, C. Hamontree, T. Nachaithong, S. Nijpanich, K. Pattarith, A novel of WS_2–$MoCuO_3$ supported with graphene quantum dot as counter electrode for dye-sensitized solar cells application, Sci. Rep. 13 (2023) 7762, https://doi.org/10.1038/s41598-023-34637-3.

[26] Q. Wu, R. Chen, P. Su, D. Shi, Y. Zhang, K. Chen, H. Li, Co_9S_8/NC@$FeCoS_2$/NC composites with hollow yolk shell structure as the counter electrode for Pt-free dye-sensitized solar cells, Electrochim. Acta 438 (2023) 141587, https://doi.org/10.1016/j.electacta.2022.141587.

[27] M. Zambrzycki, R. Piech, S.R. Raga, M. Lira-Cantu, A. Fraczek-Szczypta, Hierarchical carbon nanofibers/carbon nanotubes/NiCo nanocomposites as novel highly effective counter electrode for dye-sensitized solar cells: a structure-electrocatalytic activity relationship study, Carbon 203 (2023) 97–110, https://doi.org/10.1016/j.carbon.2022.11.047.

[28] V.T. Srisuvetha, S. Karthikeyan, P. Sangeetha, E.G. Sumangali, M. Shkir, V.R.M. Reddy, I.M. Ashraf, W.K. Kim, T. Sumathi, A highly porous MgO entrenched MWCNT composite as a low-cost Pt-free counter electrode for dye-sensitized solar cells and visible light photocatalytic performance towards Congo-red, J. Sol. Gel Sci. Technol. 106 (2023) 590–601, https://doi.org/10.1007/s10971-023-06071-4.

[29] Y. He, G. Yue, J. Huo, C. Dong, G. Xie, F. Tan, A dye-sensitized solar cells with an efficiency of 10.01% based on the MoP/$MoNiP_2$@Ti_3C_2 composite counter electrode, Materials Today Sustainability 22 (2023) 100329, https://doi.org/10.1016/j.mtsust.2023.100329.

[30] N. Kanjana, W. Maiaugree, T. Lunnoo, P. Laokul, I. Chaiya, A. Ruammaitree, P. Wongjom, Y. Infahsaeng, One-step hydrothermal synthesis and electrocatalytic properties of MoS_2/activated carbon composite derived from shallots, J. Appl. Electrochem. (2023), https://doi.org/10.1007/s10800-023-01921-z.

[31] N. Kanjana, S. Pimsopa, W. Maiaugree, P. Laokul, I. Chaiya, A. Chingsungnoen, P. Poolcharuansin, N. Ratchapolthavisin, W. Jarernboon, P. Wongjom, Y. Infahsaeng, Novel micro-ceramic bottom ash mixed PEDOT:PSS/PVP for a low-cost Pt-free counter electrode in a dye sensitized solar cell, J. Electrochem. Soc. 169 (2022) 083503, https://doi.org/10.1149/1945-7111/ac86fa.

[32] N. Kanjana, W. Maiaugree, P. Poolcharuansin, P. Laokul, Synthesis and characterization of Fe-doped TiO_2 hollow spheres for dye-sensitized solar cell applications, Mater. Sci. Eng. B 271 (2021) 115311, https://doi.org/10.1016/j.mseb.2021.115311.

[33] M. Łach, K. Korniejenko, M. Hebdowska-Krupa, J. Mikuła, The effect of additives on the properties of metakaolin and fly ash based geopolymers, MATEC Web Conf. 163 (2018) 1–8, https://doi.org/10.1051/matecconf/201816306005.

[34] T.A. Saleh, G.I. Danmaliki, Infuence of acidic and basic treatments of activated carbon derived from waste rubber tires on adsorptive desulfurization of thiophenes, J. Taiwan Inst. Chem. Eng. 60 (2016) 460–468, https://doi.org/10.1016/j.jtice.2015.11.008.

[35] Y. Liu, X. Liu, W. Dong, L. Zhang, Q. Kong, W. Wang, Efcient adsorption of sulfamethazine onto modifed activated carbon: a plausible adsorption mechanism, Sci. Rep. 7 (2017) 12437, https://doi.org/10.1038/s41598-017-12805-6.

[36] M. Veerapandian, N. Lévaray, M.H. Lee, S. Giasson, X. Zhu, Glucosamine-anchored graphene oxide nanosheets: fabrication, ultraviolet irradiation, and electrochemical properties, ACS Appl. Mater. Interfaces 7 (2015) 14552–14556, https://doi.org/10.1021/acsami.5b00608.

[37] S.A. Khan, I. Uddin, S. Moeez, A. Ahmad, Fungus-mediated preferential bioleaching of waste material such as fly-ash as a means of producing extracellular, protein capped, fluorescent and water soluble silica nanoparticles, PLoS One 9 (2014), https://doi.org/10.1371/journal.pone.0107597.

[38] C.A. Stevenson, J.E. Monroe, C.G. Norris, A.R. Roginski, S.P. Beaudoin, The effects of surface and particle properties on van der Waals (vdW) adhesion quantified by the enhanced centrifuge method, Powder Technol. 392 (2021) 514–523, https://doi.org/10.1016/j.powtec.2021.07.028.

[39] C. Henry, J.P. Minier, G. Lefèvre, Towards a description of particulate fouling: from single particle deposition to clogging, Adv. Colloid Interface Sci. 185–186 (2012) 34–76, https://doi.org/10.1016/j.cis.2012.10.001.

[40] J. Zhou, D.H. Anjum, L. Chen, X. Xu, I.A. Ventura, L. Jiang, G. Lubineau, The temperature-dependent microstructure of PEDOT/PSS films: insights from morphological, mechanical and electrical analyses, J. Mater. Chem. C 2 (2014) 9903–9910, https://doi.org/10.1039/C4TC01593B.

[41] T.H. Meen, K.L. Chen, Y.H. Chen, W.R. Chen, D.W. Chou, W.H. Lan, C.J. Huang, The effects of dilute sulfuric acid on sheet resistance and transmittance in poly (3,4-thylenedioxythiophene): poly(styrenesulfonate) films, Int. J. Photoenergy 2013 (2013), https://doi.org/10.1155/2013/843410.

[42] R. Gangopadhyay, B. Das, M.R. Molla, How does PEDOT combine with PSS? insights from structural studies, RSC Adv. 4 (2014) 43912, https://doi.org/10.1039/C4RA08666J.

[43] M. Yuan, T. L, Q. Shi, J. Dong, Understanding the KOH activation mechanism of zeolitic imidazolate framework-derived porous carbon and their corresponding furfural/aceticacid adsorption separation performance, Chem. Eng. J. 428 (2022) 132016, https://doi.org/10.1016/j.cej.2021.132016.

[44] J. Qu, Y. Wang, X. Tian, Z. Jiang, F. Deng, Y. Tao, Q. Jiang, L. Wang, Y. Zhang, KOH-activated porous biochar with high specific surface area for adsorptive removal of chromium (VI) and naphthalene from water: Affecting factors, mechanisms and reusability exploration, J. Hazard Mater. 401 (2021) 123292, https://doi.org/10.1016/j.jhazmat.2020.123292.

[45] J. Romanos, M. Beckner, T. Rash, L. Firlej, B. Kuchta, P. Yu, G. Suppes, C. Wexler, P. Pfeifer, Nanospace engineering of KOH activated carbon, Nanotechnology 23 (2012) 015401, https://doi.org/10.1088/0957-4484/23/1/015401.

[46] J.M. Kim, S.W. Rhee, Electrochemical properties of porous carbon black layer as anelectron injector into iodide redox couple, Electrochim. Acta 83 (2012) 264–270, https://doi.org/10.1016/j.electacta.2012.07.107.

[47] W. Ahmad, M.R. Al bahrani, Z. Yang, J. Khan, W. Jing, F. Jiang, L. Chu, N. Liu, L. Li, Y. Gao, Extraction of nano-silicon with activated carbons simultaneously from rice husk and their synergistic catalytic effect in counter electrodes of dye-sensitized solar cells, Sci. Rep. 6 (2016) 39314, https://doi.org/10.1038/srep39314.

[48] R. Riaz, M. Ali, T. Maiyalagan, A.A. Arbab, A.S. Anjum, S. Lee, M.J. Ko, S.H. Jeong, Activated charcoal and reduced graphene sheets composite structure for highly electro-catalytically active counter electrode material and water treatment, Int. J. Hydrogen Energy 45 (2020) 7751–7763, https://doi.org/10.1016/j.ijhydene.2019.06.138.

[49] Y. Cao, K. Wang, X. Wang, Z. Gu, Q. Fan, W. Gibbons, J.D. Hoefelmeyer, P.R. Kharel, M. Shrestha, Hierarchical porous activated carbon for supercapacitor derived from corn stalk core by potassium hydroxide activation, Electrochim. Acta 212 (2016) 839–847, https://doi.org/10.1016/j.electacta.2016.07.069.

[50] K.C. Sun, A.A. Memon, A.A. Arbab, I.A. Sahito, M.S. Kim, S.Y. Yep, Y.O. Choi, Y.S. Kim, S.H. Jeong, Electrocatalytic porous nanocomposite of graphite nanoplatelets anchored with exfoliated activated carbon filler as counter electrode for dye sensitized solar cells, Sol. Energy 167 (2018) 95–101, https://doi.org/10.1016/j.solener.2018.04.002.

[51] Q. Wang, S. Ito, M. Gratzel, F. Francisco-Santiago, I. Mora-Sero, J. Bisquert, T. Bassho, H. Imai, Characteristics of high efficiency dye-sensitized solar cells, J. Phys. Chem. B 110 (2006) 25210–25221, https://doi.org/10.1021/jp064256o.

[52] S. Sarker, H.W. Seo, D.M. Kim, Electrochemical impedance spectroscopy of dye-sensitized solar cells with thermally degraded N719 loaded TiO_2, Chem. Phys. Lett. 585 (2013) 193–197, https://doi.org/10.1016/j.cplett.2013.08.101.

[53] N. Punbusayakul, S. Talapatra, L. Ci, W. Surareungchai, P.M. Ajayan, Double-walled carbon nanotube electrodes for electrochemical sensing, Electrochem. Solid State Lett. 10 (2007) 13–17, https://doi.org/10.1149/1.2709398.

[54] C.P. Hsu, K.M. Lee, J.T.W. Huang, C.Y. Lin, C.H. Lee, L.P. Wang, S.Y. Tsai, K.C. Ho, EIS analysis on low temperature fabrication of TiO_2 porous films for dye-sensitized solar cells, Electrochim. Acta 53 (2008) 7514–7522, https://doi.org/10.1016/j.electacta.2008.01.104.

[55] M.F. Don, P. Ekanayake, H. Nakajima, A.H. Mahadi, C.M. Lim, Improvement of dye-sensitized solar cell performance through introducing TiO_2 in acetylene carbon black-graphite composite electrode, Thin Solid Films 706 (2020) 138042, https://doi.org/10.1016/j.tsf.2020.138042.
[56] S. Sarker, A.J. Saleh Ahammad, H.W. Seo, D.M. Kim, Electrochemical impedance spectra of dye-sensitized solar cells: Fundamentals and spreadsheet calculation, Int. J. Photoenergy 2014 (2014), https://doi.org/10.1155/2014/851705.
[57] Y. Zhang, S. Yun, C. Wang, Z. Wang, F. Han, Y. Si, Bio-based carbon-enhanced tungsten-based bimetal oxides as counter electrodes for dye-sensitized solar cells, J. Power Sources 423 (2019) 339–348, https://doi.org/10.1016/j.jpowsour.2019.03.054.
[58] J.M. Kim, W. Kwon, S.W. Rhee, Electrochemical properties of poly(3,4-ethylenedioxythiophene):poly (styrenesulfonate) and carbon black composite as an electron injector into the electrolyte containing iodide redox couple, Electrochim. Acta 161 (2015) 205–211, https://doi.org/10.1016/j.electacta.2015.02.091.
[59] J. Huo, M. Zheng, Y. Tu, J. Wu, L. Hu, S. Dai, A high performance cobalt sulfide counter electrode for dye-sensitized solar cells, Electrochim. Acta 159 (2015) 166–173, https://doi.org/10.1016/j.electacta.2015.01.214.
[60] H.W. Zheng, X. Liang, Y.H. Yu, K. Wang, X.A. Zhang, B.Q. Men, C.L. Diao, C.X. Peng, G.T. Yue, $Bi_5FeTi_3O_{15}$ nanofibers/graphene nanocomposites as an effective counter electrode for dye-sensitized solar cells, Nanoscale Res. Lett. 12 (2017) 18, https://doi.org/10.1186/s11671-016-1799-5.
[61] M. Wu, X. Lin, A. Hagfeldt, T. Ma, Low-cost molybdenum carbide and tungsten carbide counter electrodes for dye-sensitized solar cells, Angew. Chem. Int. Ed. 50 (2011) 3520, https://doi.org/10.1002/anie.201006635.
[62] I.T. Chiu, C.T. Li, C.P. Lee, P.Y. Chen, Y.H. Tseng, R. Vittal, K.C. Ho, Nanoclimbing-wall-like $CoSe_2$/carbon composite film for the counter electrode of a highly efficient dye-sensitized solar cell: a study on the morphology control, Nano Energy 22 (2016) 594–606, https://doi.org/10.1016/j.nanoen.2016.02.060.